Naval Surface Warfare Center
Carderock Division
West Bethesda, MD 20817-5700

Numerical Simulation of Tip Vortices of a Ducted Rotor

by

Cheng-I Yang
Minyee Jiang
Christopher J. Chesnakas
Stuart D. Jessup

20040920 122

BEST AVAILABLE COPY

REPORT DOCUMENTATION PAGE

Form Approved
OMB No. 0704-0188

1. AGENCY USE ONLY (Leave Blank)	2. REPORT DATE September 2004	3. REPORT TYPE AND DATES COVERED

4. TITLE AND SUBTITLE
Numerical Simulation of Tip Vortices of a Ducted Rotor.

5. FUNDING NUMBERS
1-5080-262-52

6. AUTHOR(S)
Cheng-I Yang, Minyee Jiang, Christopher J. Chesnakas
Stuart D. Jessup

7. PERFORMING ORGANIZATION NAME(S) AND ADDRESS(ES)
Propulsion and Fluid Systems Department, Code 5400
NSWC, Carderock Division
9500 MacArthur Blvd.
West Bethesda, MD 20817-5700

8. PERFORMING ORGANIZATION REPORT NUMBER
NSWCCD-50-TR-2004/041

9. SPONSORING / MONITORING AGENCY NAME(S) AND ADDRESS(ES)
Naval Sea Systems Command
93R
2531 Jefferson Davis Hwy
Arlington, VA 22242-5160

10. SPONSORING / MONITORING AGENCY REPORT NUMBER

11. SUPPLEMENTARY NOTES

12.a DISTRIBUTION / AVAILIBILITY STATEMENT
Approved for Public Release, Distribution Unlimited.

12.b DISTRIBUTION CODE

13. ABSTRACT (Maximum 200 words)

A ducted rotor was tested in the 36-inch water tunnel at David Taylor Model Basin, Naval Surface Warfare Center/Carderock Division. At the blade tip, both leakage and trailing edge vortices were observed through cavitation inception. Detailed flow patterns in the vortices have been mapped with LDV technique. Numerical calculations, based on a Reynolds-averaged Navier-Stokes formulation, were performed to simulate the observed vortices. To reduce the numerical diffusion, a fifth-order-accurate upwind differencing scheme was implemented to evaluate the flux difference across the cell surface. The results were compared with the experimental data.

16. SUBJECT TERMS
Navier-Stokes Solver, ducted rotor, Tip Leakage Vortex, trailing edge vortex, cavitation inception.

15. NUMBER OF PAGES
29

16. PRICE CODE

17. SECURITY CLASSIFICATION OF REPORT UNCLASSIFIED	18. SECURITY CLASSIFICATION OF THIS PAGE UNCLASSIFIED	19. SECURITY CLASSIFICATION OF ABSTRACT UNCLASSIFIED	20. LIMITATION OF ABSTRACT SAME AS REPORT

(THIS PAGE INTENTIONALLY LEFT BLANK)

CONTENTS

FIGURES

NOMENCLATURE

C	chord length
C_p	pressure coefficient ($\dfrac{P}{\frac{1}{2}\rho V_{ref}^2}$)
P	Static pressure
P_{ref}	Static pressure at reference point at water tunnel
P_v	Saturated vapor pressure
r	Radial distance from hub axis
R	Rotor radius
Re	Reynolds number ($V_{ref} R$) / ν
s	Distance along rotor pitch line, from trailing edge
V_{ref}	Magnitude of the circumferentally-averaged velocity ahead of the rotor, in stationary frame
x	distance from the rotor stack line, in X direction
x,y,z	Cartesian coordinate system
ρ	Density
σ_i	Cavitation inception number ($\dfrac{P_{ref} - P_v}{\frac{1}{2}\rho V_{ref}^2}$)
ν	kinematic viscosity

ABBREVIATIONS

CPU	Central Process Unit
CFD	Computational Fluid Dynamics
LDV	Laser Doppler Velocity
MSU	Mississippi State University
MUSCL	Monotone Upstream-centered Scheme for Conservation Laws
NACA	National Advisory Committee for Aeronautics
NAVSEA	Naval Sea Systems Command
NSWCCD	Naval Surface Warfare Center, Carderock Division
RANS	Reynolds Averaged Navier-Stokes
r.m.s.	Root mean square

rpm	Revolutions per minute
SGI	Silicon Graphics Incoperated
UNCLE	Unsteady Computation of fieLd Equation
cm	cente meter
ft/s	foot per second
mm	millimeter
m/s	meter per second

ABSTRACT

A ducted rotor was tested in the 36-inch water tunnel at David Taylor Model Basin, Naval Surface Warfare Center/Carderock Division. At the blade tip, both leakage and trailing edge vortices were observed through cavitation inception. Detailed flow patterns in the vortices have been mapped with LDV (LaserDoppler Velocity) technique. Numerical calculations, based on a Reynolds-averaged Navier-Stokes formulation, were performed to simulate the observed vortices. To reduce the numerical diffusion, a fifth-order-accurate upwind differencing scheme was implemented to evaluate the flux difference across the cell surface. The results were compared with the experimental data.

ADMINISTRATIVE INFORMATION

INTRODUCTION

This report is about a numerical simulation of tip vortices of a rotor operating in a duct. The results of the simulation are to be compared with the test data of rotor P-5206. The rotor has three blades, and is designed to operate in the 36-inch (91.44 cm) water tunnel for the investigation of the tip vortices cavitation of a ducted-rotor. The water tunnel is of an open jet type, the flow is discharged into a 90.0 inch (228.60 cm) plenum chamber through the nozzle. The pressure in the tunnel can be adjusted so that the cavitation inception can be investigated. The rotor is positioned such that its blade tip trailing edge is upstream of the nozzle of the open jet. Figure 1 shows the positioning of the rotor in the 36-inch water tunnel. The cylindrical tunnel wall serves as the duct for the rotor. The detailed rotor geometry and the test conditions are given in Reference [1], only some relevant geometrical dimensions will be mentioned briefly in the following. The rotor blade has a constant chord length of 15.0079 inches (38.12 cm) and maximum section thickness of 1.50 inches (3.81 cm). The diameters of the rotor, its hub and the inner surface of the duct are 33.475 inches (85.03 cm), 13.846 inches (35.17 cm) and 34.0 inches

(86.36 cm), respectively. The skew angles at the root and at the tip are -4 degree and 30 degree, respectively. The ratio of the tip gap to the maximum section thickness is 0.175. The axial distance between the trailing edges of the nozzle and the blade tip is 6.27 inches (15.93 cm). The rotor was driven from upstream. The velocity measurements behind the rotor were conducted with a three-component LDV system. The system consisted of two TSI model 9832 fiber optic probes rigidly mounted together on a traverse that could translate in the axial, vertical, and horizontal directions. The detailed techniques used to measure and analyze the flow field were presented in Reference [2].

Recently two numerical calculations about the tip vortices of propeller P-5206 were reported. One of the calculations, based on a finite-volume approach with artificial compressibility algorithm [3], was by Brewer [4]; and the other, based on a finite-differencing approach with pressure implicit split operator algorithm, was by Kim [5]. The former calculation was supported by an unstructured topology while the latter calculation was supported by a structured topology with overset capability derived from CHIMERA scheme [6]. Both calculations used upwind method to evaluate the convective terms. However, in the former case, the differential system is hyperbolic and the upwind direction was determined by the signs of the eignvalue of the system; while in the latter case, the upwind direction was determined by the sign of the convecting vectors, since the differential system is elliptic in nature. Despite of the distinct differences in algorithm and scheme, both calculations yield similar and excellent results in certain aspects. This report presents the results of a third calculation. The solution scheme is similar to Brewer's [4], except that the calculations were supported with a structured rather than an unstructured topology. Although the unstructured topology is more robust in generating the supporting grid system and the grid can be easily refined at where it is needed the most, it has been reported that the flow field near the solid boundary, where most of the vorticity is generated, are predicted better with a structured grid topology. Perhaps, it is because the structured grid can better resolve the laminar sub-layer near the solid surface. Overset topology [5] eliminates many difficulties associate with the grid generation and improves grid quality about complicated geometry; however interpolations are needed in order to communicate between the various overset grid systems, and interpolations often introduce errors.

Present calculations are complementary with the two mentioned above. The solver used is the UNCLE code [7], and the grid topology is structured in nature. The structured computational grid topology used here is designed such that it is able to resolve the separated flow near the blade tip and it can easily be refined to support the passage of the vertical flow. Calculations based on two different grid sizes were performed. The first calculation was exploratory; its goal is to obtain an assessment about the fidelity of the solutions, such as the

pressure and the helicity (dot product of vorticity and velocity vectors) distributions about the core of the vortices. Thrust and torque of the rotor blade should be predicted reasonably well. The goal of the second calculation is to study the sensitivity of the solutions with respect to the grid refinement. Based on the trajectory of the tip vortices of the first calculation, the grid was then refined to produce the second set of the grid for the refined calculation. The grid sizes are about 3.0 and 5.5 millions nodes for the first and the second set, respectively. In addition to the standard MUSCL scheme (monotone upstream-centered scheme for conservation laws) provided by UNCLE code [7], a third-order and a fifth-order weighted MUSCL schemes are implemented. This is an effort to reduce the numerical diffusion in the vortex core region.

The calculated flow quantities such as velocity components, helicity are compared with the measured values and the pressure distribution in vortex core is compared with previous computations.

DESCRIPTION OF THE EXPERIMENT

The detailed description and setup of the experimental facility and the offset of the blade section can be found in references [1] and [2]. The rotating speed of the rotor was 500 rpm; the tunnel speed was 22.85 f/s (6.96 m/s). The Reynolds number based on tunnel speed and the rotor radius was 3.019 million. Flow into the rotor was measured in the duct at a distance of 0.361 rotor radius upstream of the rotor stack line. The inflow was almost free of the tangential component, and the axial component of the inflow is shown in Figure 2. The thickness of the boundary layer near the duct surface is much larger then the tip gap of 0.015R. The rotor tip is well imbedded in the inflow boundary layer. Measurements of all three components of the velocity were made in the tip-vortex region just downstream of the rotor tip at 103 different x-r planes. Figure 3 indicates the location of the measuring planes, with only every tenth plane is shown. The measuring planes are normal to the pitch line at rotor tip. The last measuring plane is about half of a chord length from the rotor trailing edge. Each measuring plane was divided into a 39 x 33 mesh, in x and r direction, respectively. At each mesh point approximately 100 measurements of particle velocity were collected.

The uncertainty of the measurements depends on the sample size, the flow gradient and the turbulence level. It also depends on the ability to control the tunnel and the rotor speed. The maximum uncertainty of the axial velocity in rotating frame occurs in the vortex core and in the blade wake, they are 10% and 5% of the tunnel inflow velocity V_{ref}, respectively. The uncertainty

in the freestream is less than 1%. The uncertainty in the inception cavitation number, σ_i was estimated at 10%.

NUMERICAL SCHEME

The numerical solver used in present simulations is based on the CFD code UNCLE developed at MSU. It is based on a three-dimensional incompressible Navier-Stokes equation expressed in the conservative law form. The equations are coupled with the continuity equation through the artificial compressibility. The diffusive terms are discretized with a central differencing scheme, and the convective terms are discretized with the Roe's flux-difference splitting scheme [8]. For the steady state simulation, a first order Euler backward approximation is used to represent the time derivative. To accommodate the rotational motion, the equations of motion are first formulated in a rotating coordinate system attached to the moving body, but are then recast in the absolute-flow variables. Such formulation is popular in turbomachinery applications [9,10]. It is believed that such formulation allows more accurate calculation of flux in the finite volume method [9].

The Navier-Stokes equations of the three-dimensional, time dependent, incompressible flow can be written in a curvilinear coordinate and in a strongly conservative law form as

$$\left(\frac{Q}{J}\right)_t + (E - E_v)_\varepsilon + (F - F_v)_\eta + (G - G_v)_\varsigma = 0 \tag{1}$$

where $Q = (\rho, u, v, w)^T$

$$\text{and} \begin{bmatrix} E \\ F \\ F \end{bmatrix} = \begin{bmatrix} \dfrac{\varepsilon_x}{J} & \dfrac{\varepsilon_y}{J} & \dfrac{\varepsilon_z}{J} \\ \dfrac{\eta_x}{J} & \dfrac{\eta_y}{J} & \dfrac{\eta_z}{J} \\ \dfrac{\varsigma_x}{J} & \dfrac{\varsigma_y}{J} & \dfrac{\varsigma_z}{J} \end{bmatrix} \begin{bmatrix} E^* \\ F^* \\ G^* \end{bmatrix} \tag{2}$$

with the inviscid fluxes

$$E^* = \left(\beta u, u^2 + p, uv, uw\right)^T$$

$$F^* = \left(\beta v, uv, v^2 + p, vw\right)^T \tag{3}$$

$$G^* = \left(\beta w, uw, vw, w^2 + p\right)^T$$

and shear fluxes

$$E_v, F_v, G_v$$

β is the artificial compressibility which connects the continuity equation with the momentum equation, J is the transformation Jacobian which relates the physical domain to the computational domain, and $\varepsilon_x, \varepsilon_y, \varepsilon_z, \eta_x, \eta_y, \eta_z, \zeta_x, \zeta_y, \zeta_z$ are the transformation metrics.

In order to apply Roe's concept of flux differencing to the convective and pressure differentiation terms, the Reynolds number is assumed high and approaching infinite. The shear fluxes $\left(E_v, F_v, G_v\right)$ are then relatively small in comparison with their corresponding inviscid fluxes $\left(E, F, G\right)$. It can then be assumed that the waves that travel across a cell face are normal to the face. Subsequently the three-dimensional system of partial differential equations is spatially split into three quasi one-dimensional conservative laws

$$\left(\frac{Q}{J}\right)_t + H_\theta = 0,\tag{4}$$

where θ is ε, η, or ζ, and H is E, F, or G. Defining computational cells with their centroids at m (m=i, j, or k), and their cell interfaces at m±1/2, an implicit discrete approximation to Equation 4 can be written as

$$\left[\left(\frac{I}{\tau J}\right) + D_m \Delta_m\right]\Delta Q^n + \Delta_m H^n = 0,\tag{5}$$

where τ is time step size, $\Delta Q^n = Q^{n+1} - Q^n$ and $\Delta_m H = \left[H_{m+1/2} - H_{m-1/2}\right]/\Delta\theta$ and $D = \partial H/\partial Q$ the flux Jacobian. For the construction of an approximate Riemann solver for the initial value problem in Equation 5, the flux at the cell interface m+1/2 that separates the right from the left traveling wave, can be define as

$$H_{m+1/2}^n = H_m^n + \left(\Delta H_{m+1/2}^-\right)^n,\tag{6}$$

or

$$H_{m+1/2}^n = H_{m+1}^n - \left(\Delta H_{m+1/2}^+\right)^n,\tag{7}$$

or the simple average of Equations 6 and 7. At present calculation, Equation 6 is used, since it has less operation count. In Equations 6 and 7, the superscript – and + of the flux differencing term represents the right and the left traveling wave across the interface m+½, respectively. That is

$$\left(\Delta H_{m+1/2}^{-}\right)^{n} = \left[R\Lambda^{-}R^{-1}(Q_{m+1}^{R} - Q_{m}^{L})\right]^{n}, \tag{8}$$

and

$$\left(\Delta H_{m+1/2}^{+}\right)^{n} = \left[R\Lambda^{+}R^{-1}\left(Q_{m+1}^{R} - Q_{m}^{L}\right)\right]^{n}, \tag{9}$$

with R, R^{-1} represent right and left eignvector of the eigen system of flux Jacobian D, respectively, Λ^{+}, Λ^{-} represent positive and negative eigen value of the system, respectively, and Q_{m+1}^{R}, Q_{m}^{L} represent the dependent variable to the right and the left of the interface, respectively. For the first order approximation, $Q_{m+1}^{R} = Q_{m+1}$ and $Q_{m}^{L} = Q_{m}$.

To evaluate the Equation 6 numerically, a Roe's [8] mean value matrix $D_{m+1/2} = D(Q_{m}, Q_{m+1})$ is introduced with the following properties;

$$D_{m+1/2}\Delta_{m+1/2}Q = \Delta H_{m+1/2}, \tag{10}$$

and

$$D(Q_{m}, Q_{m+1}) = D_{m}, \quad \text{if } Q_{m} \rightarrow Q_{m+1}. \tag{11}$$

The conditions in Equations 10 and 11 are to ensure that the solution to Equation 5 is conservative in space. For the incompressible flow, the only state of the dependent variable Q that satisfies these properties is the simple average of the Q_{m+1}^{R}, and Q_{m}^{L}. Accordingly, the first term on the right hand side of the Equation 6, H_{m}^{n}, is computed with the metrics evaluated at the interface m+½ and the dependent variable Q evaluated at centroid m, that is $Q=Q_{m}^{L}$. For the second term on the right hand side of the Equation 6, $(\Delta H_{m+1/2}^{-})^{n}$, the eignvectors and the eignvalues R, R^{-1}, Λ^{-}, are evaluated with the metrics and the dependent variable defined at the interface m+½, that is $Q=\frac{1}{2}\left(Q_{m+1}^{R} + Q_{m}^{L}\right)$.

To enhance the accuracy of the solution, Van Leer's [11] MUSCL (monotone upstream-centered scheme for conservation laws) approach is adopted. The dependent variables to the right and to the left of the interface of the cell are reconstructed as

$$Q^R_{m+1/2} = Q_{m+1} - \tfrac{\varphi}{4} \left[(1-\kappa)(Q_{m+2} - Q_{m+1}) - (1+\kappa)(Q_{m+1} - Q_m)\right], \qquad (12)$$

and

$$Q^L_{m+1/2} = Q_m + \tfrac{\varphi}{4} \left[(1-\kappa)(Q_m - Q_{m-1}) + (1+\kappa)(Q_{m+1} - Q_m)\right]. \qquad (13)$$

If $\varphi = 0$, the Equations 12 and 13 recover the first order approximation. If $\varphi = 1$ and $\kappa = -1$, the approximation is second order. If $\varphi = 1$ and $\kappa = 1/3$, the approximation is third order. An alternative approach to the reconstruction is to apply the stencil shown in Equations 12 and 13 to the characteristic variables W in the computational space, where $W = R^{-1}Q$. Once $W^R_{m+1/2}$ and $W^L_{m+1/2}$ are obtained, the independent variables $Q^R_{m+1/2}$ and $Q^L_{m+1/2}$ can be recovered by pre-multipling $W^R_{m+1/2}$ and $W^L_{m+1/2}$ with the right eignvector R computed at the interface m+1/2. This reconstruction process, identified here as weighted MUSCL here, requires higher operation count, but it takes the coordinate non-uniformity and stretching into account. The scheme described here, has been used to compute the flow in linear cascade with tip clearance[12]. Similarly, a fifth order stencil, suggested by Rai [13] and used by Rogers and Kwak [14], is derived and applied to the characteristic variables here. That is

$$W^R_{m+1/2} = W_{m+1} + \tfrac{1}{60}[+2\Delta_{m+5/2}W - 11\Delta_{m+3/2}W - 24\Delta_{m+1/2}W + 3\Delta_{m-1/2}W] \qquad (14)$$

and

$$W^L_{m+1/2} = W_m + \tfrac{1}{60}[-2\Delta_{m-3/2}W + 11\Delta_{m-1/2}W + 24\Delta_{m+1/2}W - 3\Delta_{m+3/2}W] \qquad (15)$$

The weighted MUSCL schemes described here are implemented in UNCLE code for present calculations.

The numerical viscous fluxes defined in Equation 1 can be obtained through central differencing technique. The differencing equations that represent the Navier-Stokes equation formulated in conservation form can then be assembled. The system of equations is solved with Newton iteration method. Standard $\kappa\varepsilon$ type turbulence equation is used for turbulence simulation.

GRID GENERATION

The inflow to the rotor is assumed axisymmetrical; therefore, only one blade passage, bounded between two adjacent blades, with appropriated boundary condition is sufficient for the numerical simulation. The water tunnel, as shown in Figure 1, is an open jet type, with jet discharging into a plenum from the tunnel nozzle downstream of the rotor. At current simulation, the plenum is not modeled, and the tunnel is assumed to extend downstream with constant radius, with no-slip boundary condition applied on its wall. In the blade passage, a half C-type grid is

used to wrap around the pressure side and suction side of the blade, covering the volume immediately around the blade surface. The rest of the volume, extended 4.5 rotor radius both upstream and downstream from the stacking line, including the tip gap, is represented by the H-type grid. The C-type grid wrapping around the blade is to provide a better grid quality near the leading edge. The first grid point off the blade surface is about five millionth of the blade radius, at the testing Reynolds number (3.1 millions, based on the tunnel speed and blade radius), the corresponding y^+ is about 2. Based on the topology just described, two grids with different nodal numbers are generated. The coarse grid has about 2.8 million nodes and the fine grid has about 5.5 million nodes. The grid system is then divided into ten connecting blocks for multi-processors processing.

COMPUTATIONAL RESULTS

The computations were performed on SGI 3400 multi-processing machines. The solutions were interpolated onto the measurement planes for the purpose of comparisons with the experimental data. The velocity profile shown in Figure 2 was used as upstream inflow for present computation. The reference static pressure was fixed to zero at far field downstream.

Figure 4 shows the formation of the tip vortices from the computation based on the coarse grid. The flow enters the tip gap region from the pressure side of the blade and vorticity is generated and convected in the gap region. As the flow exits to the pressure side, the roll-up begins. As the flow exits near the leading edge, the vortex rolls up and forms the core of the leakage vortex. The flow exits around the mid-chord and after rolls up and wraps around the core. At the trailing edge, the flow from the tip gap merges with the flow from the pressure side and the flow from the suction side and forms the trailing edge vortex. The trailing edge vortex then wraps around the leakage vortex. The region of the depression of the static pressure coincides with the passage of the vortex core.

Figure 5 shows the contours of the computed static pressure at various x-r planes behind the trailing edge. There are three sets of images in Figure 5. The image (a) is based on the coarse grid with standard MUSCL scheme; the images (b) and (c) are based on fine grid with third and fifth order weighted MUSCL schemes, respectively. Comparison of the three images indicates that the pressure distribution is less diffusive when finer grid or higher order differencing scheme is employed.

One way to trace the vortex in the three-dimensional flow field is through the display of helicity, which is the projection of the velocity vector V onto the vorticity vector ϖ , that

is $H = V \bullet \varpi$. Figure 6 shows the helicity downstream of tip trailing edge. The image (a) is the computed helicity with the third order weighted MUSCL scheme based on the fine grid, the image (b) is the helicity derived from the measurement. Based on the intensity of the helicity, it can be seen from both the computation and measurement that at a distance about 10% chord length downstream of the trailing edge, the trailing edge vortex crosses over and wraps around the leakage vortex. At that location, the computed helicity is slightly less than measured. The contours displayed in Figure 6 suggest that the computed trajectory of the vortex center is slightly further away from the suction side than measured.

Figure 7 to Figure 12 show the tangential velocity vectors and streamwise vorticity contours on the x-r planes at a distance of -0.0108, 0.0596, 0.0920, 0.1245 and 0.3032 chord length from the trailing edge, respectively. The tangential velocity is obtained by projecting the velocity vector onto the x-r plane and the streamwise vorticity is obtained by dividing the helicity with the magnitude of the velocity. In each of those figures, two images are presented. The image on the left is derived from the experimental data and the image on the right is from the computational results. Figure 7 shows that at the immediately upstream of the trailing edge, the vorticity is concentrated in the leakage vortex and in the shear layer that exits the gap. The vorticity in the shear layer feeds into the leakage vortex continuously; in the meantime, the viscous diffusion takes place. Those two competing elements determine the strength of the vorticity in the vortex. The locations of the computed and the measured centers of vortex, estimated by the orientation of the tangential velocity vectors and the intensity of the vorticity, match quite well. However, the intensity of the computed streamwise vorticity is lower than the measured. The discrepancy may be caused by the grid resolution in the region of vortex passage. In a earlier vortex simulation, it was found that to resolve the cross section of the vortex core accurately, a 20 by 20 mesh is needed. At present, the average mesh size in core region is about 10 by 10.

Figure 8 shows that at a distance of 6% chord length downstream of the trailing edge, in addition to the leakage vortex, a trailing edge vortex appears. Its present can be seen by the intense vorticity concentration above the leakage vortex. Figure 9 and Figure 10 show that the trailing edge vortex wraps around the leakage vortex, as it convects further downstream. At this stage, the predicted trajectory of the vortex center becomes further away from the blade suction surface than the one measured. Figure 11 and Figure 12 show that at further downstream from trailing edge, at s/C = 0.3010 and s/C = 0.4037, the trailing edge vortex becomes very weak and undistinguishable.

Figure 13 to Figure 17 show the computed tangential velocity vectors and static pressure contours on the x-r planes at a distance of 0.0%, 10%, 20%, 30% and 40% chord length

downstream from the trailing edge. The results are based on: (a) coarse grid with the standard MUSCL scheme, (b) fine grid with the standard MUSCL scheme, (c) fine grid with the weighted MUSCL scheme, and (d) fine grid with the fifth-order MUSCL scheme. Through the pressure contours, Figure 14 indicates that at s/C=0.1026 the trailing edge vortex is better resolved with weighted MUSCL scheme, especially with the fifth-order accuracy.

Figure 18 shows the computed static pressure distribution in the vortex core. Results presented are based on both coarse and fine grids, with MUSCL and weighted MUSCL schemes. For the purpose of comparison, Iowa-Kim's result is also presented [5]. The reference pressure for present calculations is set at zero at downstream exit. This is compatible with Kim's approach [5]. For all the calculations, the minimum static pressure within the flow field occurs at a distance about 11% chord length downstream of the trailing edge where the trailing edge vortex is crossing over the leakage vortex and begins the wrapping around process. Overall, at a given location, the fine grid calculation produces lower vortex core pressure than the coarse grid calculation; the weighted MUSCL scheme produces lower vortex core pressure than the standard MUSCL scheme, and the fifth order differencing scheme produces even lower level of pressure. The computed minimum static pressure on blade surface is about -4.0, and is located on the suction side of the blade tip, about 80% chord length from the leading edge. This concurs with Kim's finding [5].

In general, at a given x-r plan, the location of minimum pressure coincides with that of the vortex center. With the same differencing scheme, the solution of the fine grid gives lower vortex core pressure than the solution of the coarse grid. With the same grid, the solution of the weighted scheme gives lower vortex core pressure than the solution of the unweighted scheme. The fifth-order differencing scheme gives the lowest vortex core pressure. The pressure differentiations among the computations mentioned above take place only within the vortex core where the gradients of velocity and pressure are sharp. In the region away from the vortex core, the effects of the grid density and the order of the differencing schemes are less significant.

DISCUSSION AND CONCLUSION

A successful numerical simulation of vortex flow requires higher order differencing scheme and dense grid support. At present, to simulate the vortex flow about the ducted-rotor P5206, two sets of grid with different nodal numbers (2.8 million and 5.5 million nodes) are utilized for grid sensitivity study, and a fifth-order weighted MUSCL scheme is derived and implemented to reduce the numerical diffusion in the vortex core. Numerical solutions show that

higher order differencing scheme indeed gives sharper and less diffusive static pressure and streamwise vorticity distributions within the vortex core.

Results from the fine grid and fifth-order solution show that the minimum pressure in the flow field occurs in the vortex core at about 11% chord length downstream of the tip trailing edge. This is the location where the trailing edge vortex crossing over the leakage vortex. At that location, the pressure coefficient C_p is about -10.22. According to the observation of cavitation inception, at the rotor operating condition, the cavitation index σ_i is about 11. The location of inception is about half a chord length downstream of the trailing edge. At that location, the measured helicity or streamwise vorticity do not show any unusually high values to indicate the possibility of the existence of low static pressure. The cause of the discrepancy may attribute to the unsteadiness of the vertical flow. The unsteady nature of the trailing vortices has been reported by Green [15,16,17], and Green and Acosta [18]. It has been observed that the flow in the vortex core is highly unsteady and the core pressure fluctuations are a remarkable one to two times the freestream dynamic pressure. Outside of the core, the flow unsteadiness diminishes rapidly and the measured flow unsteadiness is largely due to the freestream turbulence. It has also been observed that the region that was 0.3 to 2 chord length downstream from the trailing edge, was the most unsteady portion of the vortex core. Due to the large static pressure fluctuation, the cavitation inception occurred at mean core pressure above the vapor pressure.

In the investigation of turbulent shear cavitation, O'Hern [19] found that in the vortex core, the pressure fluctuations had positive and negative peaks as high as three times the freestream dynamic pressure, sufficient to explain cavitation inception at high values of the inception index. In summary, the flow in the vortex core is highly unsteady, especially in the region 0.3 to 2 times chord length downstream of the trailing edge. It is highly likely that the inception may occur at mean pressure higher than the vapor pressure in that region. At present computations, the minimum static pressure occurs at a distance about 0.11 chord length downstream of the trail edge, where the flow is mostly steady and Reynolds number independent. At a distance 0.5 chord length downstream of the trailing edge, the flow is mostly unsteady, and the predicted mean static pressure is -7.0. A negative pressure fluctuation of -4.0 is sufficient to cause the inception. Such a magnitude of fluctuation is likely to occur according to Green's studies[15,16,17,18].
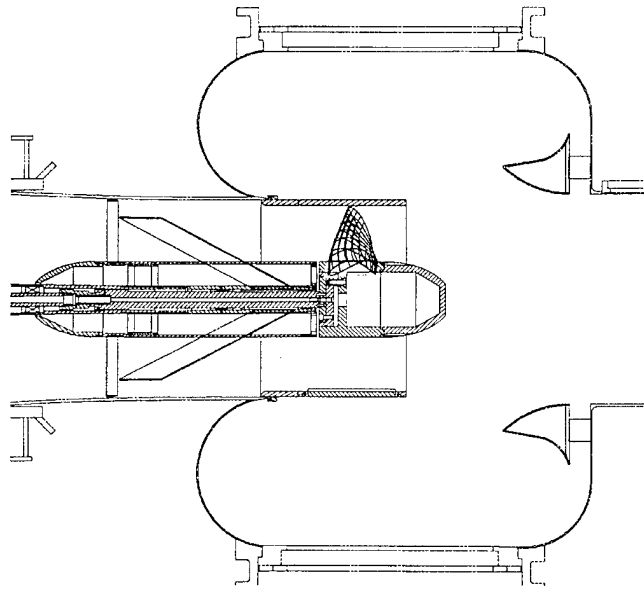
ACKNOWLEDGEMENTS
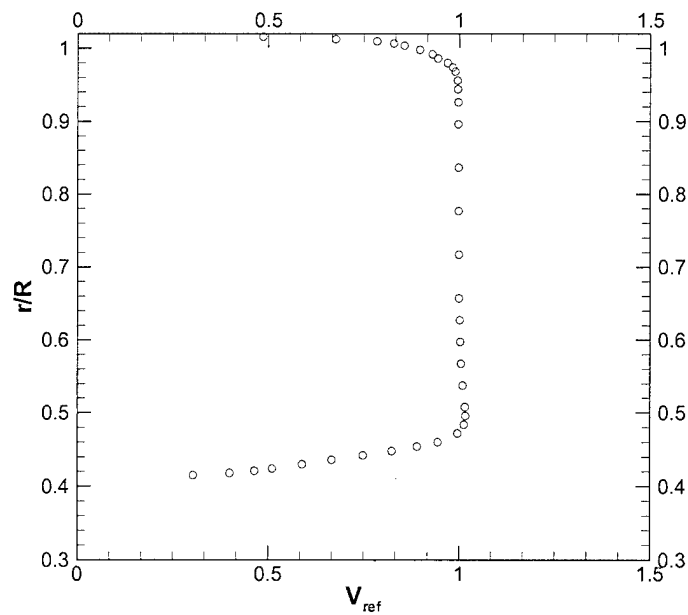
Figure 1: Rotor P5206 in 36-inch water tunnel.

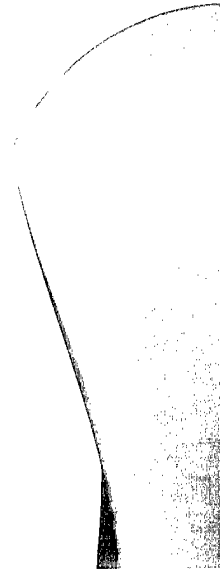Figure 2: Axial component of inflow to the rotor, measured at x/r=-0.361.
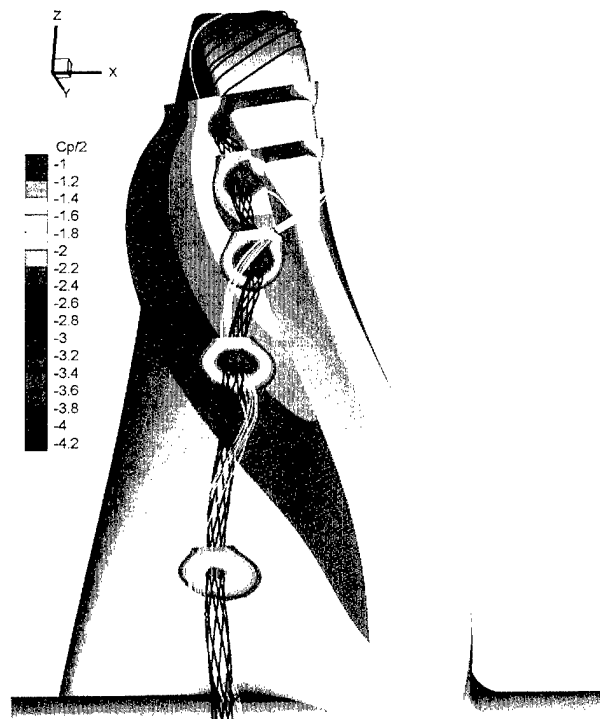
Figure 3: Planes where LDV measurements are taken.
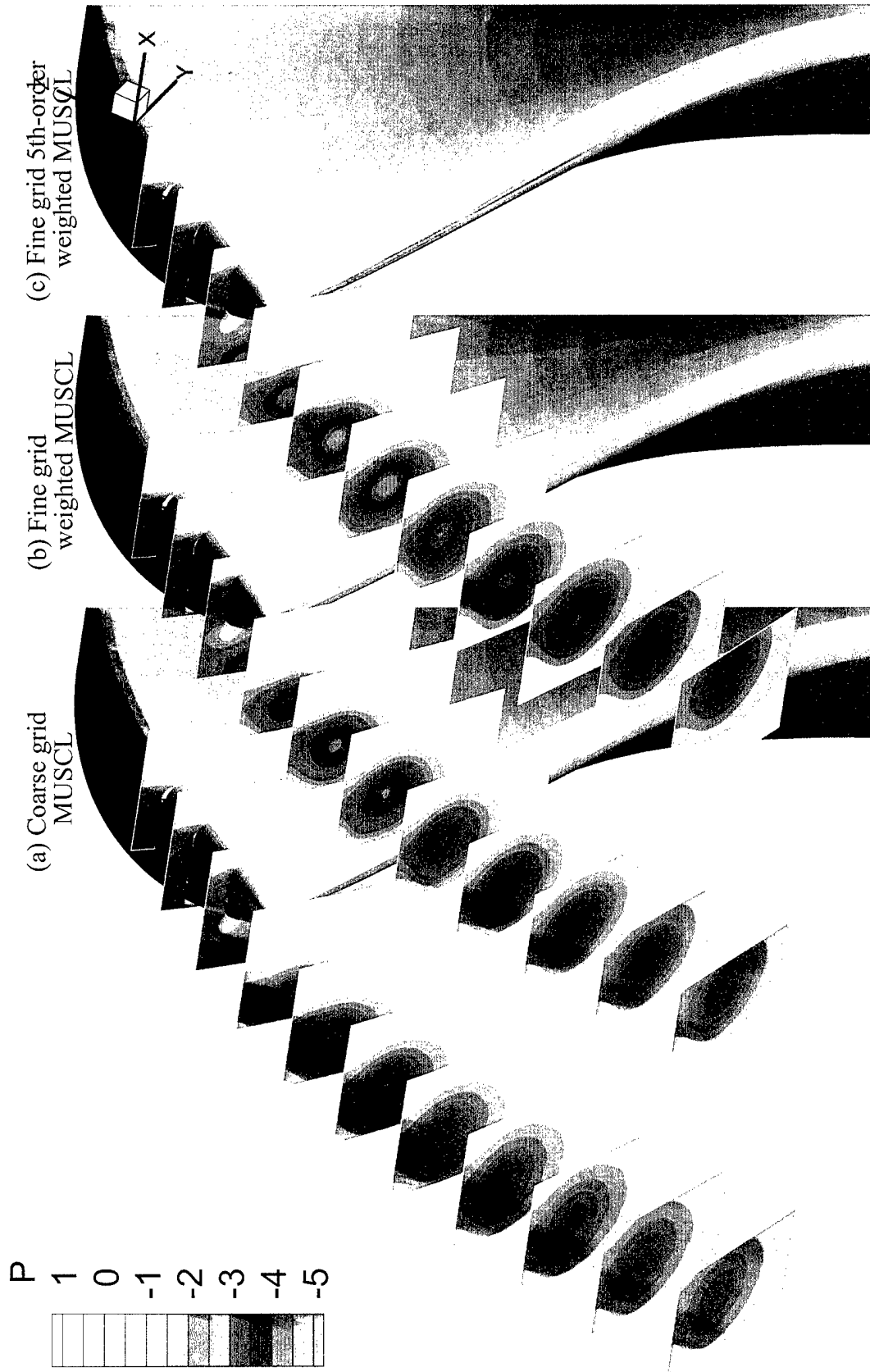

Figure 4: Formation of tip vortices.

Figure 5: Computed static pressure contour behind tip trailing edge.
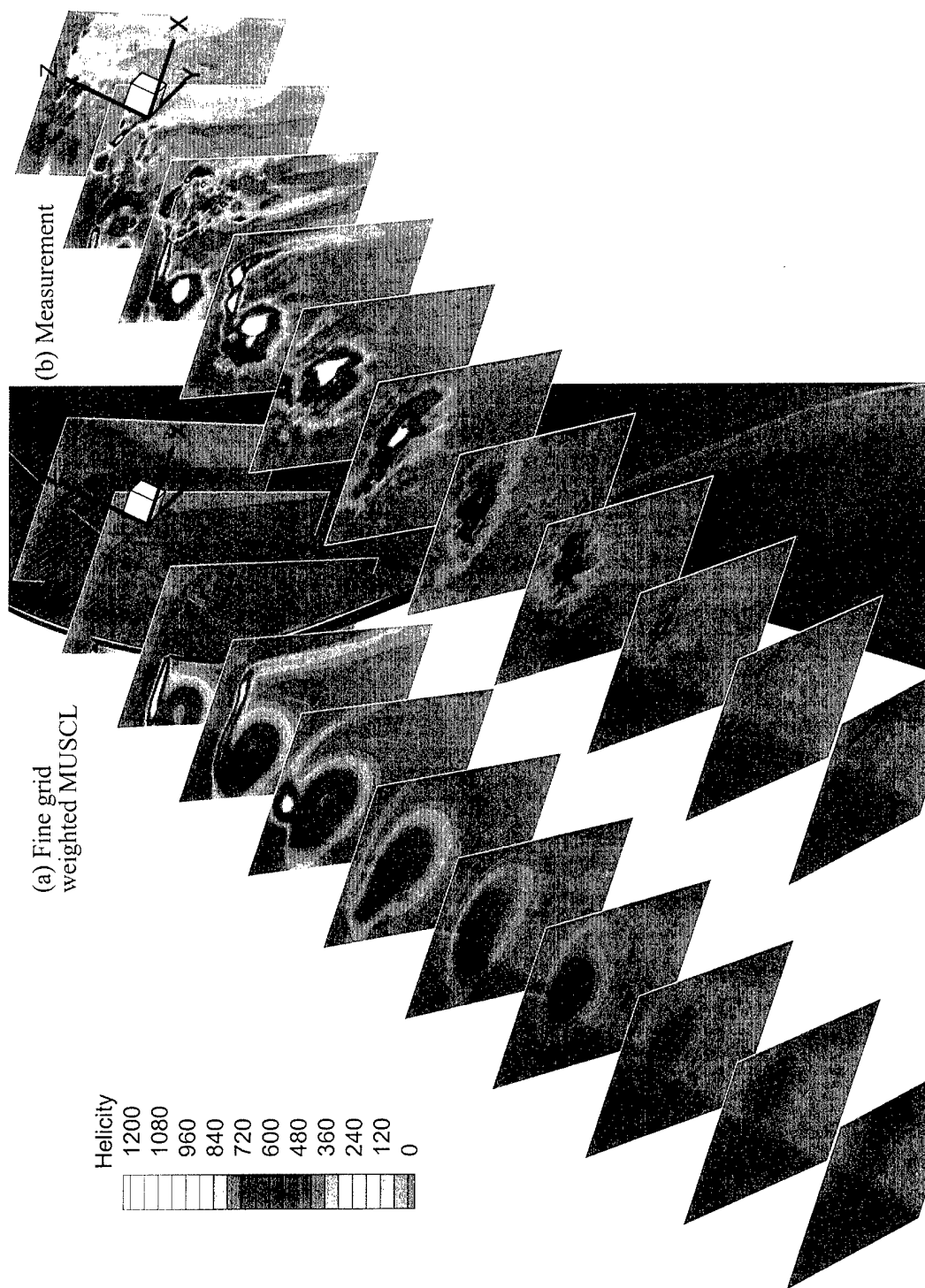
(a) Coarse grid MUSCL

(b) Fine grid weighted MUSCL

(c) Fine grid 5th-order weighted MUSCL

(a) Fine grid weighted MUSCL

(b) Measurement

Helicity
1200
1080
960
840
720
600
480
360
240
120
0

Figure 6: Comparison of computed and measured helicity.
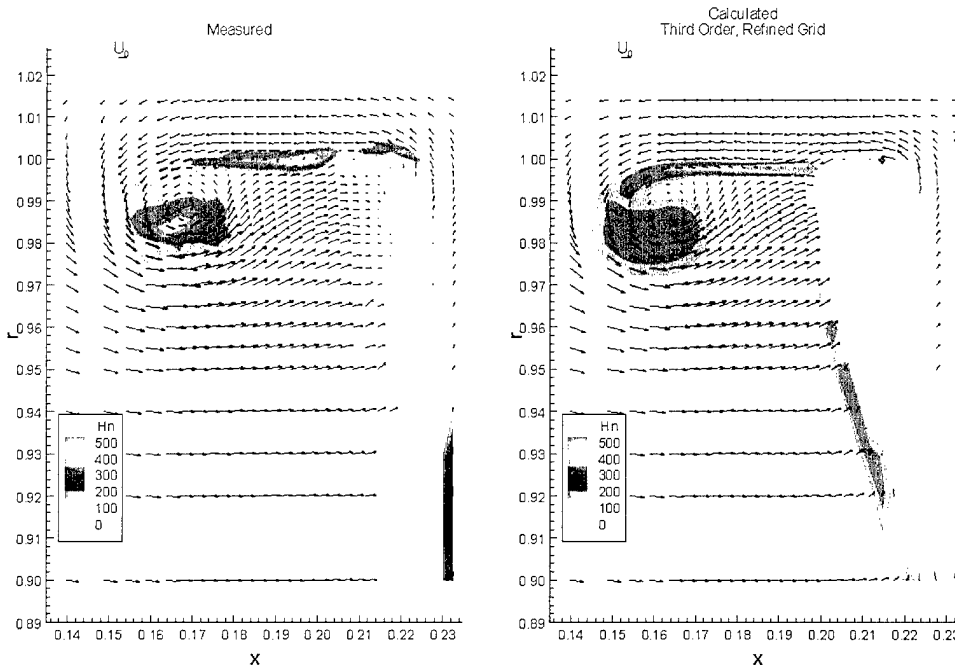
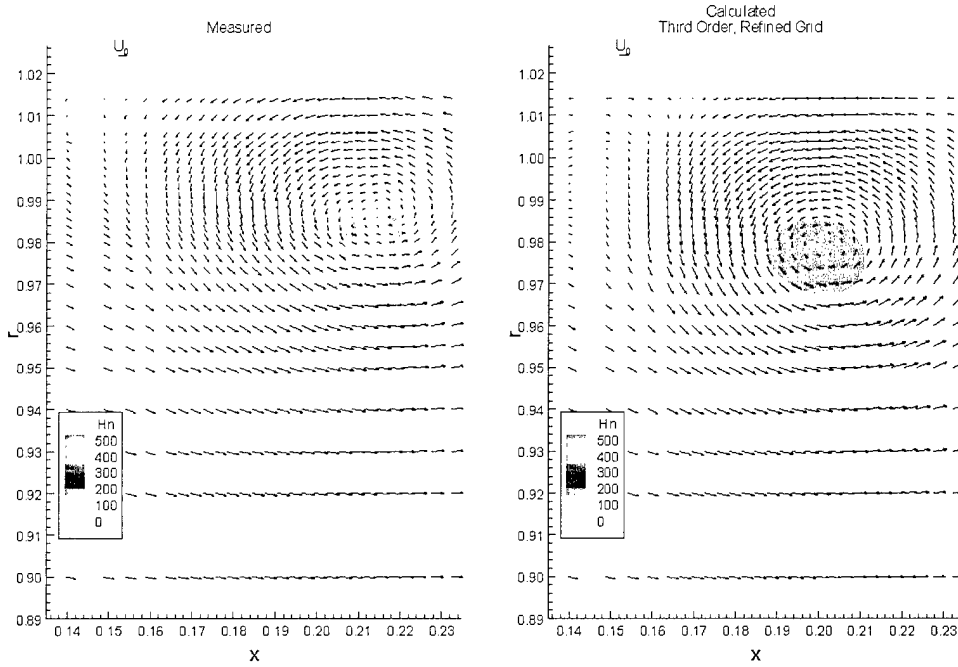Figure 7: Computed and measured tangential velocity vectors and streamwise vorticity contours at s/C=-0.0108.
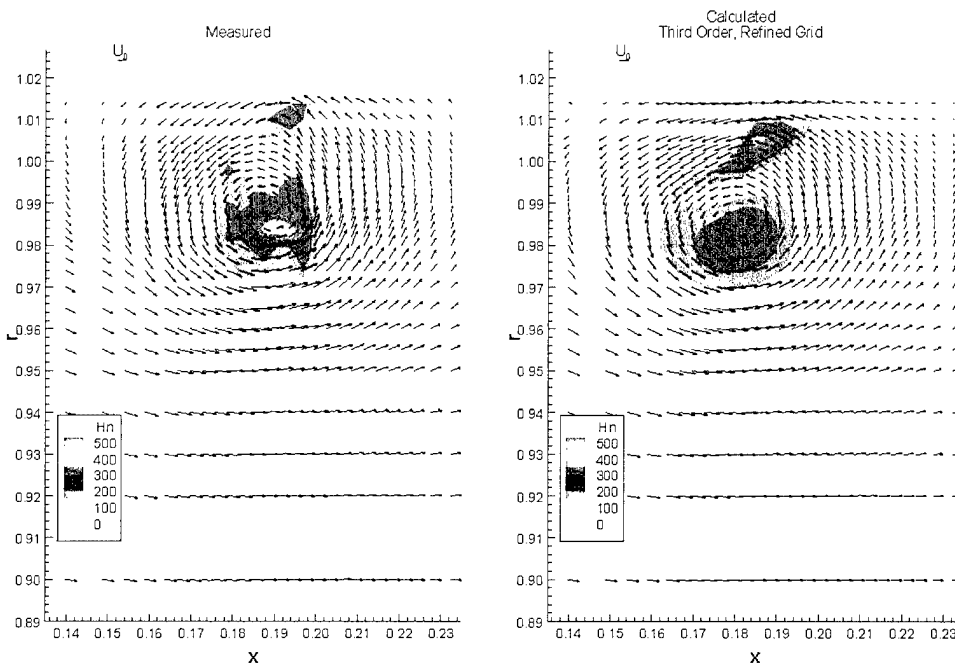
Figure 8: Computed and measured tangential velocity vectors and streamwise vorticity contours at s/C = 0.0596.

s/C = 0.0920
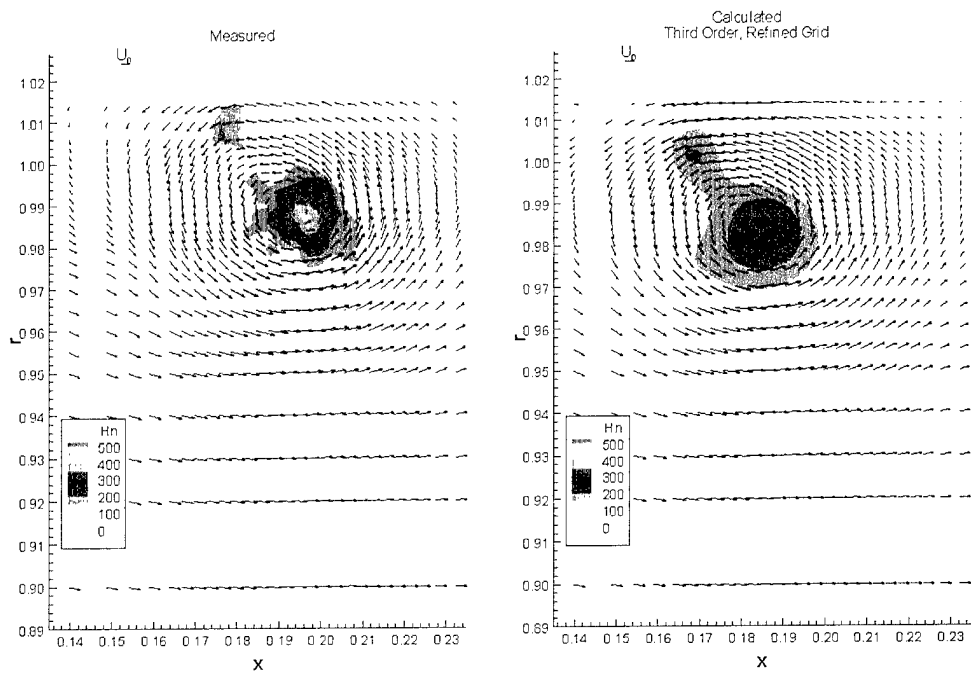
Figure 9: Computed and measured tangential velocity vectors and streamwise vorticity contours at s/C=0.0920.

s/C = 0.1245
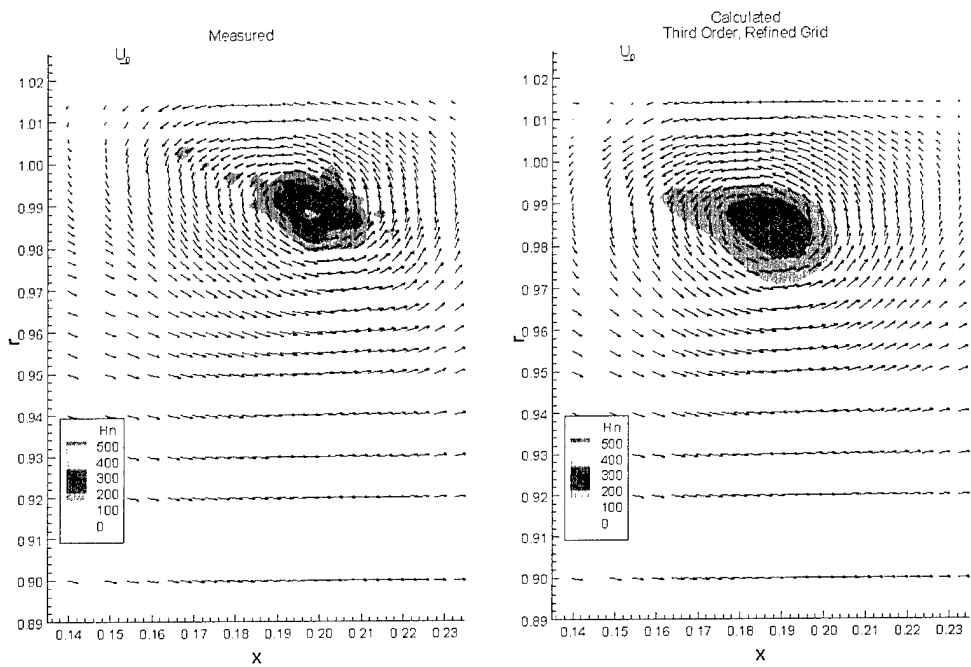
Figure 10: Computed and measured tangential velocity vectors and streamwise vorticity contours at s/C=0.1245.

Figure 11: Computed and measured tangential velocity vectors and streamwise vorticity contours at s/C=0.3032.

s/C = 0.4006

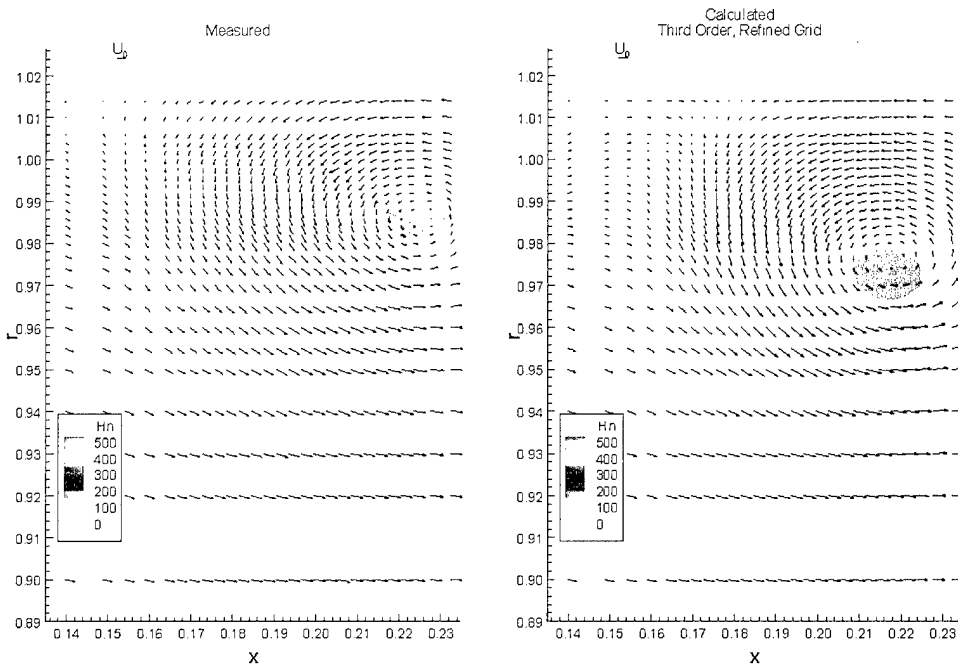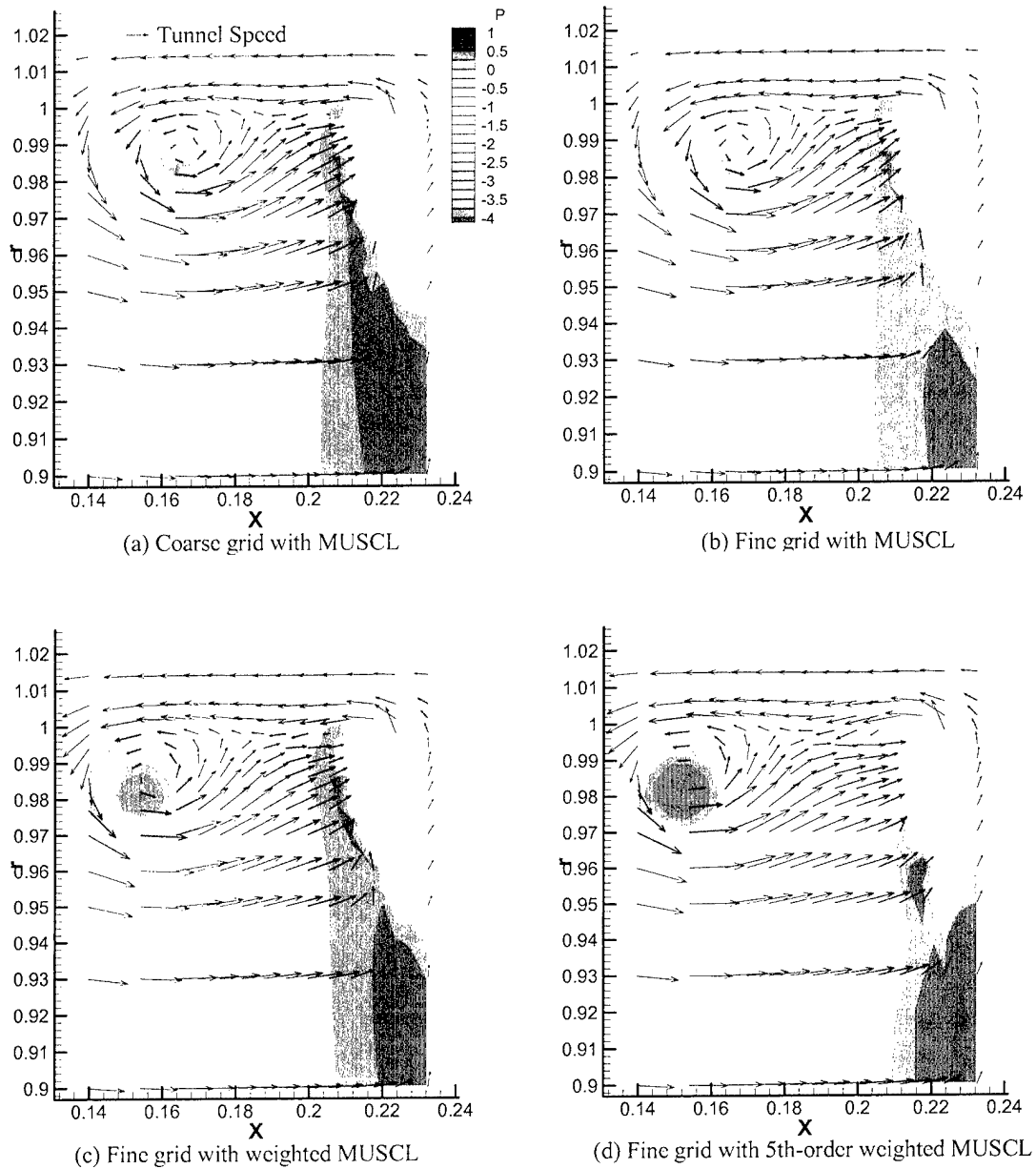Figure 12: Computed and measured tangential velocity vectors and steamwise vorticity contours at s/C=0.4006.

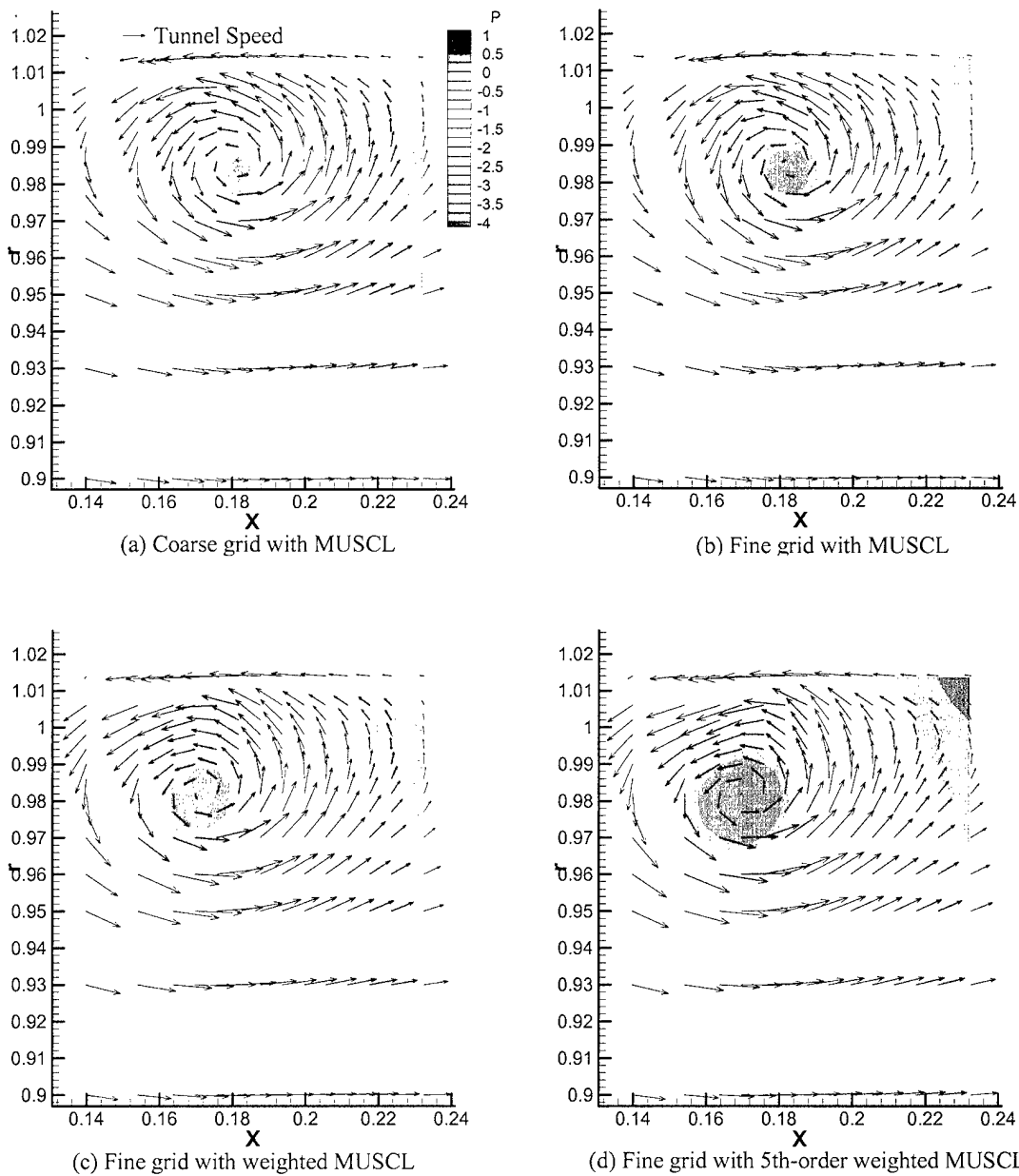Figure 13: Computed tangential velocity vectors and static pressure contours at s/C=0.000.

(a) Coarse grid with MUSCL

(b) Fine grid with MUSCL

(c) Fine grid with weighted MUSCL
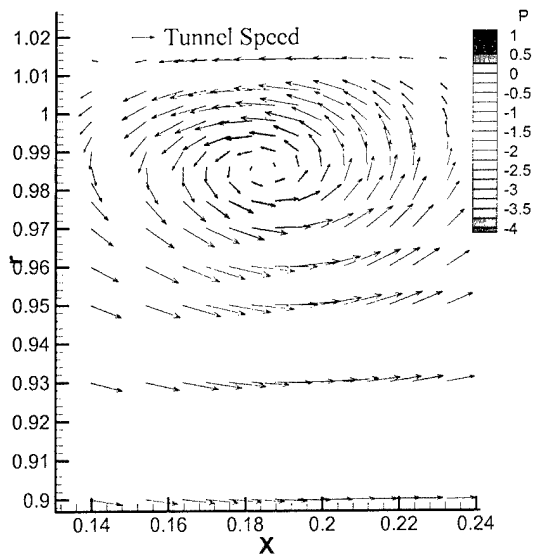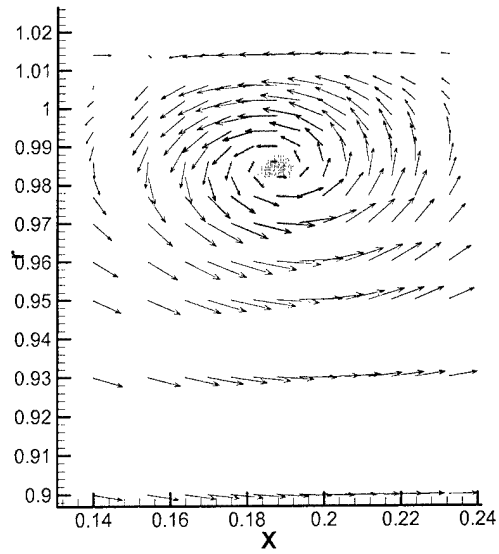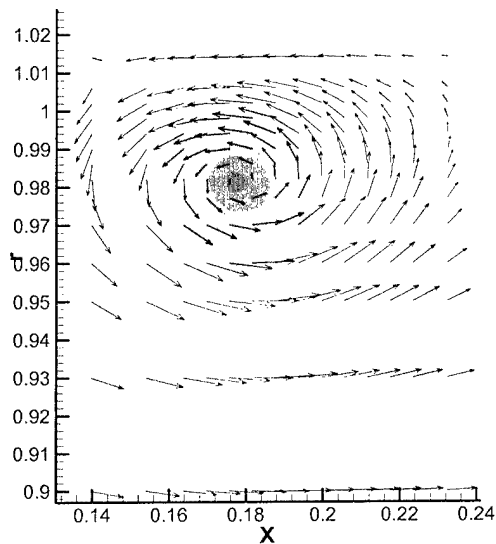
(d) Fine grid with 5th-order weighted MUSCL

Figure 14: Computed tangential velocity vectors and static pressure contours at s/C=0.1026.

(a) Coarse grid with MUSCL

(b) Fine grid with MUSCL

(c) Fine grid with weighted MUSCL

(d) Fine grid with 5th-order weighted MUSCL

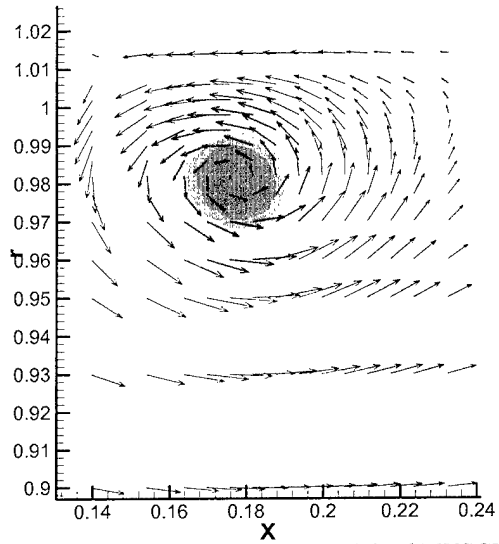Figure 15: Computed tangential velocity vectors and static pressure contours at s/C=0.2052.

(a) Coarse grid with MUSCL

(b) Fine grid with MUSCL

(c) Fine grid with weighted MUSCL
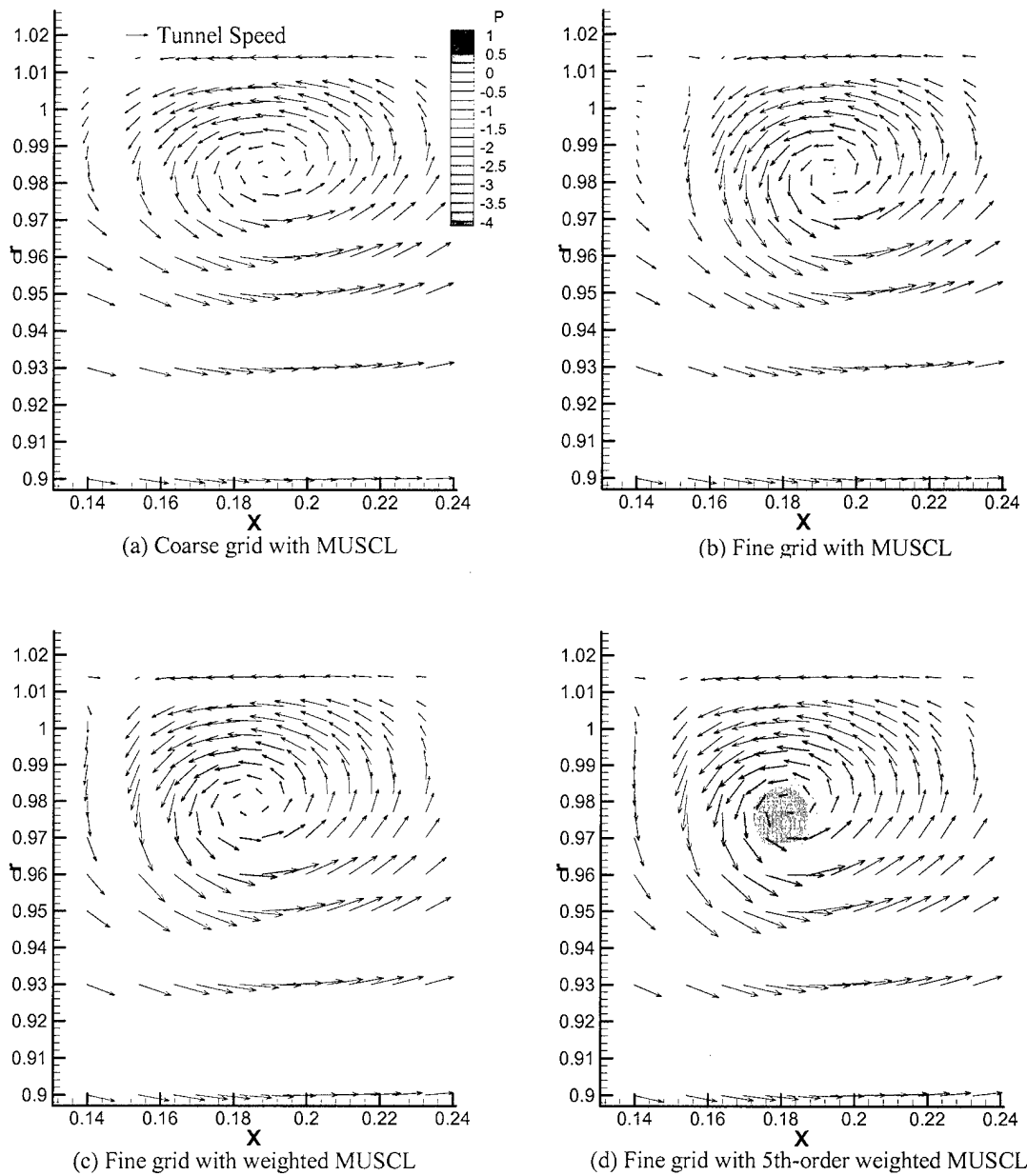
(d) Fine grid with 5th-order weighted MUSCL

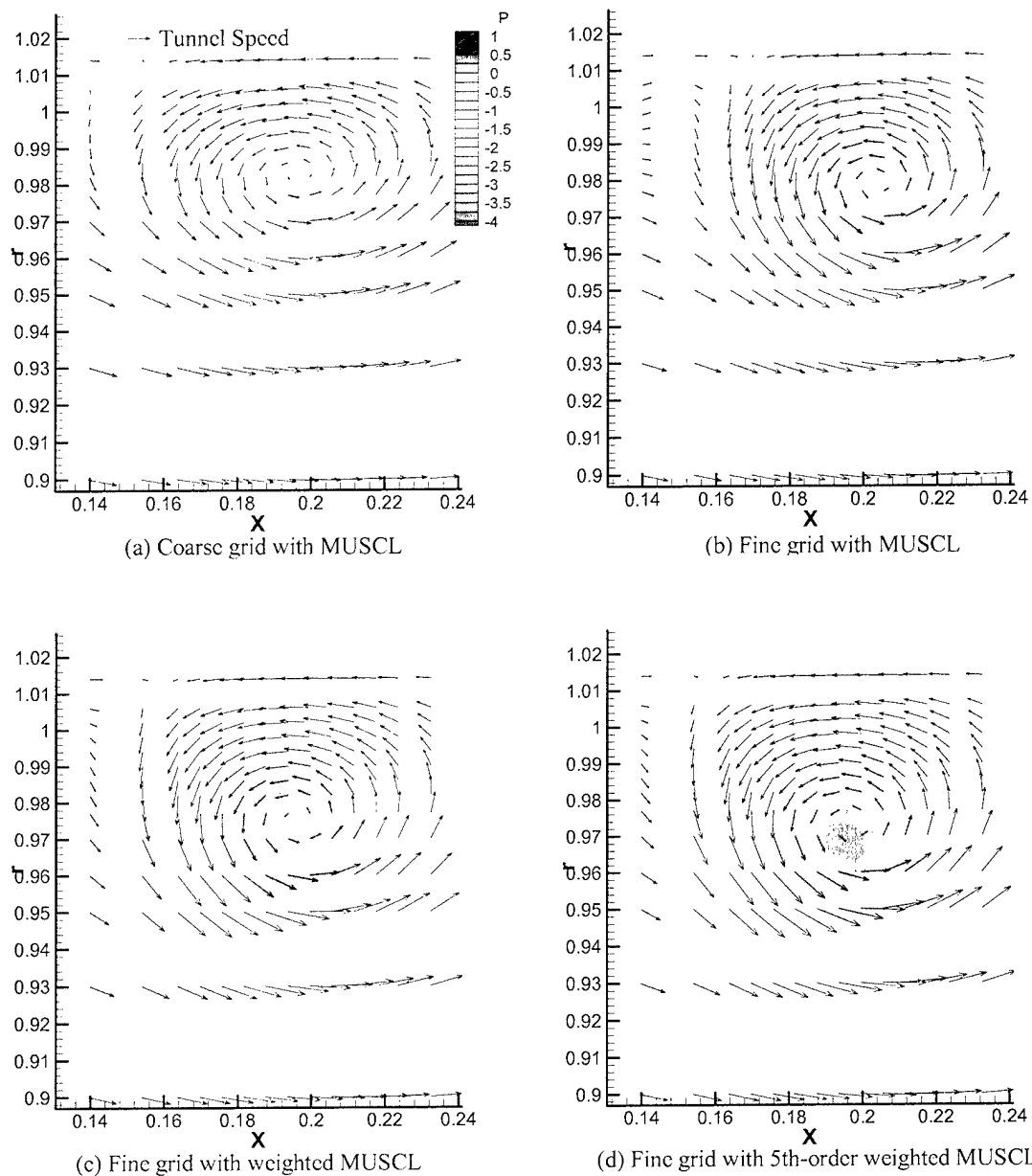Figure 16: Computed tangential velocity vectors and static pressure contours at s/C=0.3031.

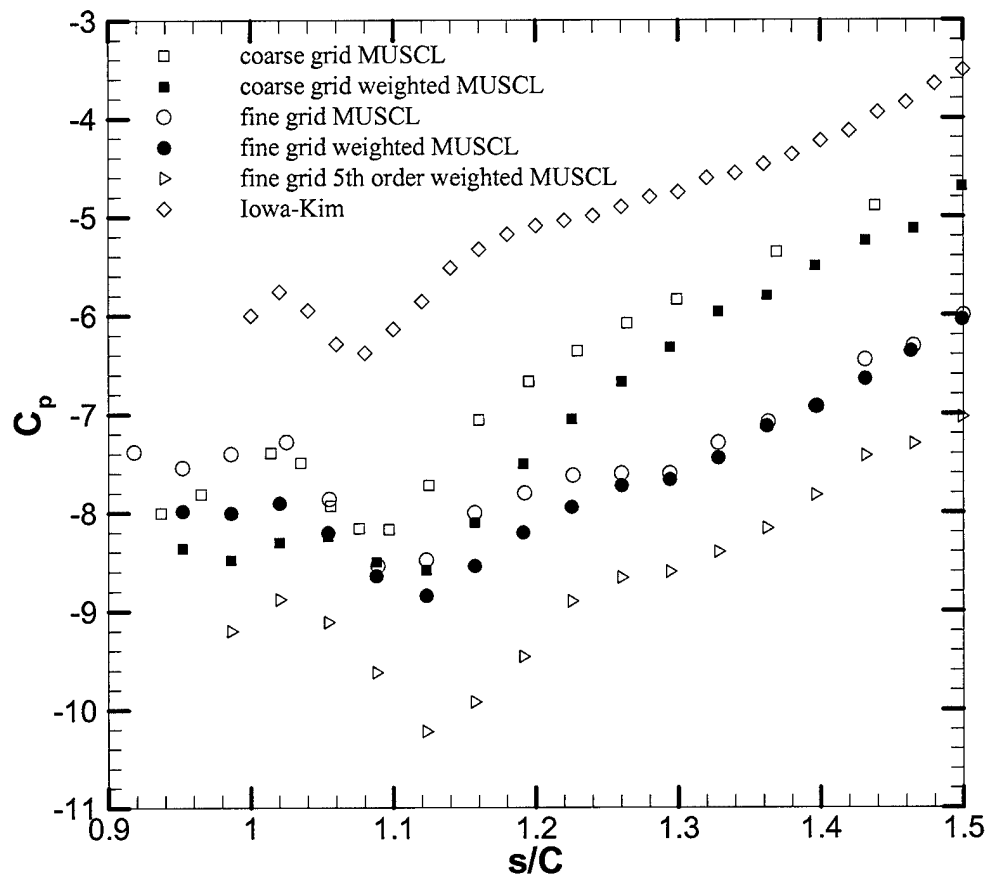Figure 17: Computed tangential velocity vectors and static pressure contours at s/C=0.4037

Figure 18: Computed static pressure distributions in vortex core.

(THIS PAGE INTENTIONALLY LEFT BLANK)

REFERENCES

1. Judge,C.Q., Oweis,G.F., Ceccio,S.L., Jessup,S.D., Chesnakas,C.J., Fry, D.J., "Tip-Leakage Vortex Inception on a Ducted Rotor." CAV2001: *4th International Symposium on Cavitaion*, Pasadena, California, USA (2001).

2. Chesnakas, C.J., Jessup, S.D., "Tip-Vortex Induced Cavitaion on a Ducted Propulsor." *Proceedings of FEDSM'03 4th ASME_JSME Joint Fluids Engineering Conference*, Honolulu, Hawaii, USA, July 6-11, 2003.

3. Chroin,A.J., "A numerical Method for Solving Incompressible Viscous Flow Problems." *Journal of Computational Physics*, Vol. 2 pp12-26. (1967).

4. Brewer,W.H., "On Simulating tip-leakage Vortex Flow to Study the Nature of Cavitation Inception." *Ph.D. thesis*, Mississippi State University. (2002).

5. Kim,J. "Sub-Visual Cavitation and Acoustic Modeling for Ducted Marine Propulsor." *Ph.D. thesis,* University of Iowa. (2002).

6. Steger,J.L., Dougherty,F.C., Benek,J.A., "A chimera Grid Scheme." Advances in Grid Generation, K.N. Ghia, U. Ghia, eds., *ASME FED*. (1983).

7. Taylor, L.K., " Unsteady Three-Dimensional Incompressible Algorithm Based on Artificial Compressibility." *Ph.D. thesis*, Mississippi State University. (1991).

8. Roe. P.L., "Approximate Riemann Solver, Parameter Vectors, and Difference Schemes," *Journal of Computational Physics*, Vol.483, No.2, pp. 357-372, (1981).

9. Agarwal, R.K., Deese, J.E., " Euler calculations for Flowfield of a Helicopter Rotor in Hover." *AIAA* 86-1782. (1986).

10. Chen,J.P., Ghosh, A.R., Sreenivas, K., Whitfield, D.L., " Comparison of Computations Using Navier-Stokes Equations in Rotation and Fixed Coordinates for Flow Through Turbomachinery." AIAA-97-0878 *35th Aerospace Sciences Meeting and Exhibit* Jan6-10, (1997), Reno,NV.

11. Anderson, W.K.,Thomas, J.L., Van Leer, B., "Comparison of Finite Volume Flux Vector Splittings for the Euler Equations." *AIAA Journal*, Vol.24,No.9, PP.14531460 (1986).

12. Yang, C-I, "Numerical Simulation of Flow in Linear Cascade with Tip Clearance." *Hydromechanics Directorate Technical Report* NSWCCD-50-TR-2000/053 (2000).

13. Rai,M.M., "Navier-Stokes Simulations of Blade-Vortex Interaction Using High-Order Accurate Upwind Scheme," AIAA Paper 87-0543, (1987).

14. Rogers,S.E., Kwak,D., "Upwind Differencing Scheme for Time-Accurate Incompressible Navier-Stokes Equations," *AIAA Journal* Vol.28., NO. 2, Feb. (1990).

15. Green, S.I., "Trailing Vortex Core Unsteadiness-an Exploratory Study of Reynolds Number effect." *AIAA/ASME National Fluid Dynamics Congress*, pp.1064-1068 (1988).

16. Green, S.I., "Tip Vortices-Single phase and Cavitating Flow Phenomena." *Ph.D. these*, California Institute of Technology, (1989).

17. Green, S.I., "Tailored Air Bubble Determination of Trailing Vortex Core Pressure." *ASME Cavitation and Multiphase Flow Forum*, San Diego. (1989).

18. Green, S.I., Acosta, A.J., "Unsteady Flow in Trailing Vortices." *Journal of Fluid Mechanics* Vol.227, pp. 107-134 (1991).

19. O'Hern, T.J., "An Experimental Investigation of Turbulent Shear Flow cavitaion." *Journal of Fluid Mechanics* Vol.215 pp. 365-391 (1990).

INITIAL DISTRIBUTION

Code	Name
NAVSEA	
93R	M. Stout
ONR	
333	K.H. Kim
333	P. Purtell
334	Meunch

CENTER DISTRIBUTION

Code	Name
50	Koh
508	J. Brown, B. Cox, R. Meyer
54	J. Gorski
54	C-I Yang
54	B Chen
54	S. Neely
54	S. Jessup
54	M. Wilson
54	C. Chesnakas
54	Y. Shen
54	R. Szwerc
5010	Office file
5060	D. Walden